crystals

MDPI

Article

Tailoring the Magnetic and Hyperthermic Properties of Biphase Iron Oxide Nanocubes through Post-Annealing

Supun B. Attanayake [1], Amit Chanda [1], Raja Das [2], Manh-Huong Phan [1] and Hariharan Srikanth [1,*]

[1] Department of Physics, University of South Florida, Tampa, FL 33620, USA; attanayake@usf.edu (S.B.A.); achanda@usf.edu (A.C.); phanm@usf.edu (M.-H.P.)
[2] SEAM Research Centre, South East Technological University, X91 K0EK Waterford, Ireland; raja.das@setu.ie
* Correspondence: sharihar@usf.edu

Abstract: Tailoring the magnetic properties of iron oxide nanosystems is essential to expanding their biomedical applications. In this study, 34 nm iron oxide nanocubes with two phases consisting of Fe_3O_4 and α-Fe_2O_3 were annealed for 2 h in the presence of O_2, N_2, He, and Ar to tune the respective phase volume fractions and control their magnetic properties. X-ray diffraction and magnetic measurements were carried out post-treatment to evaluate changes in the treated samples compared to the as-prepared samples, showing an enhancement of the α-Fe_2O_3 phase in the samples annealed with O_2 while the others indicated a Fe_3O_4 enhancement. Furthermore, the latter samples indicated enhancements in crystallinity and saturation magnetization, while coercivity enhancements were the most significant in samples annealed with O_2, resulting in the highest specific absorption rates (of up to 1000 W/g) in all the applied fields of 800, 600, and 400 Oe in agar during magnetic hyperthermia measurements. The general enhancement of the specific absorption rate post-annealing underscores the importance of the annealing atmosphere in the enhancement of the magnetic and structural properties of nanostructures.

Keywords: iron oxide nanocubes; phase tunability; magnetic hyperthermia; biomedicine

check for updates

Citation: Attanayake, S.B.; Chanda, A.; Das, R.; Phan, M.-H.; Srikanth, H. Tailoring the Magnetic and Hyperthermic Properties of Biphase Iron Oxide Nanocubes through Post-Annealing. *Crystals* **2024**, *14*, 519. https://doi.org/10.3390/cryst14060519

Academic Editor: Limei Zheng

Received: 6 May 2024
Revised: 24 May 2024
Accepted: 27 May 2024
Published: 30 May 2024

Copyright: © 2024 by the authors. Licensee MDPI, Basel, Switzerland. This article is an open access article distributed under the terms and conditions of the Creative Commons Attribution (CC BY) license (https://creativecommons.org/licenses/by/4.0/).

1. Introduction

The recent ability to fabricate magnetic structures of nanometer size, known as nanomagnetism, has allowed for the study of unique magnetic phenomena that are unobservable at larger length scales [1–4]. It has been shown that by utilizing nanostructures of varying sizes and shapes, their applicability in fields ranging from biomedicine to memory devices can be improved [2,3,5–9]. Iron oxide, one of the most historically studied magnetic systems, has been found to be a unique platform for observing the interplay between different thermodynamically stable phases and their respective magnetic orders, which has allowed for broad applications [3,10–13]. This composition, already approved by the Food and Drug Administration (FDA), is observed in many devices and has shown potential to be tuned within its iron oxide composition to multiple magnetic phases with distinct features; thus, the phase-tunability of iron oxide phases such as magnetite (Fe_3O_4), hematite (α-Fe_2O_3), maghemite (γ-Fe_2O_3), and wüstite (FeO) are currently being examined [14,15]. The phase-tunability with size of iron oxide nanostructures has shed light on the stability of certain phases in a variety of conditions, such as the FeO phase, which possesses higher stability in smaller structures measuring ~30 nm [16]. As an extension of an initial study of how the stability of iron oxide phases changes with size, different types of phase tunability in iron oxide nanostructures need to be explored. Prior research has shown that functionalizing iron oxide nanostructures for hyperthermia applications requires the tuning of their shape and size [6,17]. Of the various shapes that have previously been studied, nanocube structures measuring ~30 nm have been shown to possess elevated potential compared to other structures such as spheres [6]. This is due to their enhanced anisotropy,

which results in higher specific absorption rates (SARs) and higher contrasts in magnetic resonance imaging (MRI) in comparison to its spherical counterparts [5,6,17,18]. Nature itself has shown the importance of contemplating iron oxide nanocubes with structures such as magnetosomes which are found within magnetotactic bacteria that possess the capability to act as compasses by utilizing the Earth's magnetic field to navigate, opening up its use in further applications spanning from drug delivery to nanoelectronics [19–21].

In this study, we explored the effects of different annealing atmospheres to manipulate the phase volume and hence magnetic properties of biphase iron oxide nanocubes for biomedical applications. Nanocubes consisting of Fe_3O_4 and α-Fe_2O_3 with no observable exchange bias or superparamagnetic behavior were annealed in the presence of O_2, N_2, He, and Ar to observe compositional and magnetic changes. Herein, O_2 is a reactive gas that can directly interact with iron oxide structures, while N_2 is a comparatively less reactive gas that can facilitate reaction-stimulating environments. The latter two gases are well-known inert gases, with He being the lightest. Furthermore, the as-prepared and treated nanocubes were evaluated for their effectiveness in magnetic hyperthermia therapy, which showed that the coercivity enhancement plays a major role in tuning hyperthermia efficiency in comparison to the saturation magnetization enhancement.

2. Materials and Methods

The synthesis of iron oxide nanocubes (NCs) was carried out following the procedures put forward by Nemati et al. [6]. The chemicals Fe(III)-acetylacetonate ($Fe(acac)_3$, $\geq$99.9%), oleylamine (OA, 70%), oleic acid (OY, 90%), benzyl ether (BE, 98%), and 1,2-hexadecanediol (HDD, 90%) (Sigma-Aldrich, St. Louis, MO, USA) were uniformly mixed using a magnetic stirrer in a three-necked round-bottomed flask with a jacketed heating mantle. The side openings were dedicated to a thermometer and continuous N_2 flow, which was initially carried out with the condenser detached at the first stage to facilitate degassing for 30 min at 110 °C to ensure that moisture and air were removed from the flask. The condenser was then fitted with cold water circulation to ensure maximum retention of the reactants throughout the process. The nucleation stage was then initiated at 200 °C and lasted for 120 min, with the final reflux stage carried out for 45 min, after which the solution was allowed to reach room temperature in the absence of a heat source. The obtained turbid, reddish solution was then cleaned a minimum of two times with ethanol and a small amount of hexane. The cleaning was carried out via back-to-back sonication for ~5 min and by centrifuging the solution at 5000 revolutions per minute for 5 min; after each time, the supernatant was disposed. The obtained product was then allowed to dry down to a fine powder which was evaluated for its structural and morphological characterization using a FEI Morgagni 268 transmission electron microscope (TEM) (FEI, Hillsboro, OR, USA) operating at 60 kV; this was followed by a compositional evaluation via diffractometry using a Bruker AXS D8 X-ray diffractometer (XRD) (Bruker, Madison, WI, USA) functioning in Bragg–Brentano geometry at a Cu Kα wavelength. The obtained samples, which conformed to the initial structural and compositional evaluation, were then separated, with some kept as controls while the others were heated in the presence of multiple gases at 300 °C for 2 h in a ceramic combustion boat placed inside a tube furnace. The gases oxygen (O_2), nitrogen (N_2), helium (He), and argon (Ar) were of ultra-high purity grade and were obtained from nexAir. The treated samples were then evaluated again for their structural and morphological characterization using the TEM and XRD. All magnetic measurements were performed in a DynaCool Physical Property Measurement System (PPMS) (Quantum Design, San Diego, CA, USA), utilizing the vibrating sample magnetometer (VSM) option. Magnetic hyperthermia measurements were performed using a 4.2 kW Ambrell EasyHeat Li3542 system with varying magnetic fields (0–800 Oe) at a constant 310 kHz frequency. The samples were measured at 20 °C as the starting temperature for a period of 300 s and with 1 mg/mL of nanoparticles in a 2% by-weight agar solution prepared using deionized water.

3. Results and Discussion

3.1. Structural Characterization

The structural and morphological properties of the iron oxide nanocubes (NCs) were evaluated using ImageJ 1.53k software using the images obtained from the transmission electron microscope (TEM), which yielded a size distribution of nanocubes at 34 ± 4 nm. Furthermore, the size distribution remained statistically similar in all annealed samples. The lattice parameter "a", extracted from an X-ray diffractometry (XRD) peak analysis, was incorporated into Table 1 for the primary phase Fe_3O_4, illustrating the evolution of the crystal parameters [22,23]. The as-prepared (AP) sample in the inset of Figure 1a displays a uniform distribution of nanocubes, showing the presence of ferrimagnetic (FiM), magnetite (Fe_3O_4), and antiferromagnetic (AFM) hematite (α-Fe_2O_3), as seen in the XRD patterns. When the AP nanocubes were annealed in O_2, the appearance of distinctive **(113)** and **(024)** peaks indicated an increase in the volume fraction of the α-Fe_2O_3 phase. The exposure to N_2 removed a significant amount of the α-Fe_2O_3 volume fraction; this change signified a change in the oxidation number from 3 to 8/3 as the α-Fe_2O_3 reduced to Fe_3O_4 [24]. This reduction in the oxidation number confirms the ability of N_2 to act as a reducing agent at high temperatures and pressures [24]. The reaction, which has been reported for hematite nanowires when annealed for 1 h at 350 °C, seemed to be initiated at 300 °C in our iron oxide nanocubes when they were annealed for 2 h [25]. Here, neither inert gas showed a significant phase change from the AP nanocubes. Though significant morphological changes were absent in all samples post-annealing, a chain formation was observed in the annealed samples which is understood to be due to dipole–dipole interactions between the NCs with the annihilation of the surfactants [26]. This chain formation can be advantageous for hyperthermia treatments as it tends to increase the specific absorption rate (SAR) values with the enhancement of the anisotropic interactions [20,21,27–29].

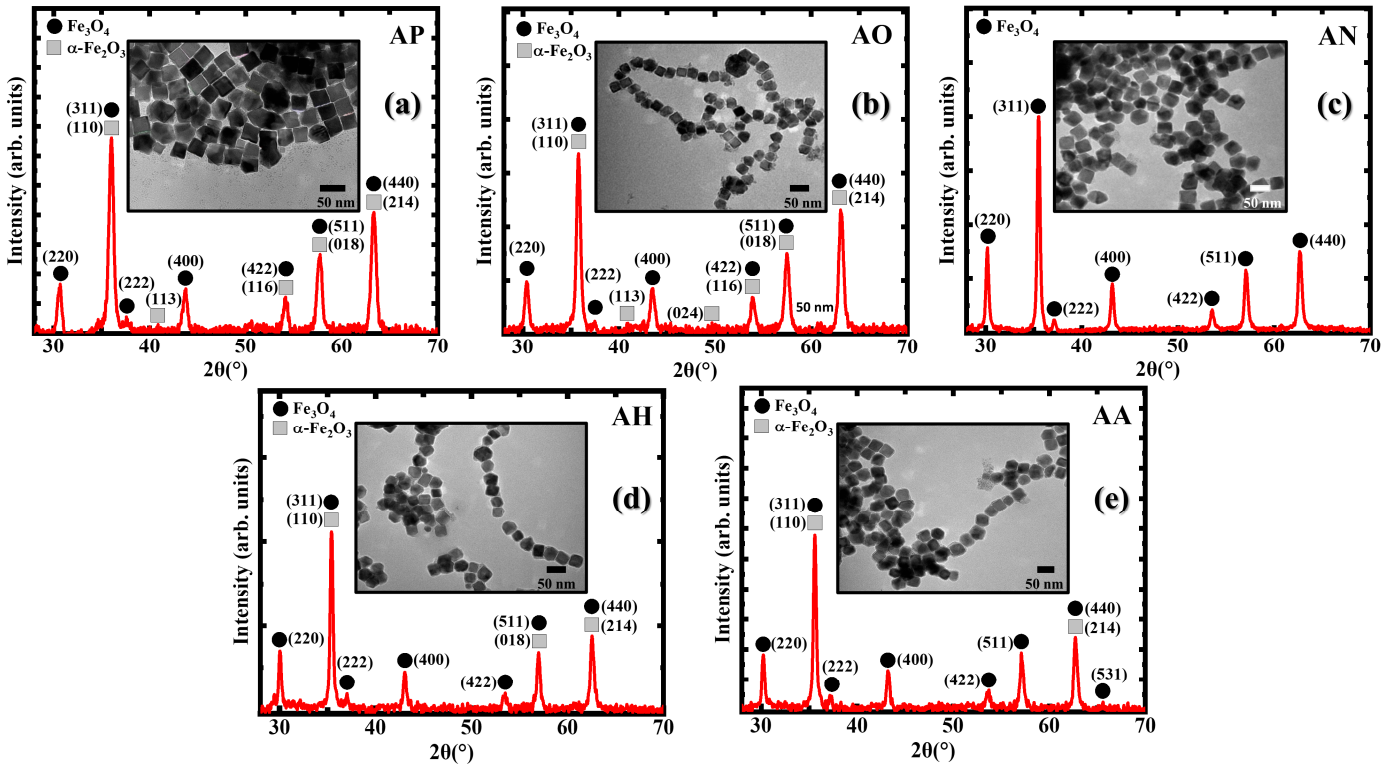

Figure 1. XRD patterns and TEM images (inset) of (**a**) the as-prepared iron oxide nanocubes, (**b**) the iron oxide nanocubes annealed in O_2, (**c**) the iron oxide nanocubes annealed in N_2, (**d**) the iron oxide nanocubes annealed in He, and (**e**) the iron oxide nanocubes annealed in Ar.

Table 1. Magnetic and lattice parameters and SAR values for all samples tested at 300 K.

Sample	H_C (Oe)	M_S (emu/g)	SAR in Agar @ 800 Oe (W/g)	Lattice Parameter (a) of Fe_3O_4 (Å)
30 nm Nanocubes [6]	33.7	67.5	~540	Not Applicable
AP	57.5	67.6	544	8.27
AO	**109**	61.2	**1001**	8.32
AN	67.1	74.3	692.8	8.37
AH	64.8	**77.6**	624.4	**8.40**
AA	80	73.8	712.3	8.37

3.2. Magnetic Properties

Temperature-dependent magnetization, M(T), measurements were carried out between 10 and 300 K following the zero-field cooled (ZFC), field-cooled cooling (FCC), and field-cooled warming (FCW) protocols in the presence of a 500 Oe magnetic field. The Verwey transition (VT), a first-order metal–insulator transition in which the crystalline phase changes from a high-temperature cubic structure to low-temperature monoclinic structure indicative of the Fe_3O_4 phase, is observed in all samples except the sample annealed in O_2 (AO) at temperatures of 109 K $\leq T_V \leq$ 121 K [30–32]. The sharpness of the transition which translates the crystallinity of the Fe_3O_4 phase can be observed to increase with annealing in the presence of N_2 (AN), He (AH), and Ar (AA), with the exception of the AO sample. The AO sample is understood to be oxidized in multiple stages simultaneous with the final products of α-Fe_2O_3, following the reaction [33,34].

The inside of the structure is expected to be oxidized to a γ-Fe_2O_3-like (or γ-Fe_2O_3) phase from Fe_3O_4 which results in the disappearance of the VT [33,35–38]. The absence of the VT observed in prior annealing on iron oxide nanorods by Attanayake et al. supports the oxidation to a γ-Fe_2O_3-like phase [35,39] The AN, AH, and AA, which indicated the reduction in the α-Fe_2O_3 phase indicated by the XRD data and the absence of the Morin transition (MT), are observed to show the transformation at comparative temperatures in the presence of various mixtures of gases, in our case, N_2, He, and Ar [40,41]. Relative to the AP sample, the MT feature became less pronounced in the annealed samples due to the increased crystallinity of the Fe_3O_4 phase. Furthermore, the AA indicates a slightly higher decrease in α-Fe_2O_3 which can be observed in the absence of **(018)** in Figure 1e and the sharpness of the VT in Figure 2d compared to AH.

The first-order magnetic transition, MT, commonly known as the temperature-driven spin–flop transition, is associated with the presence of the α-Fe_2O_3 phase which occurs as the spin alignment changes from perpendicular to the c-axis above the TM to parallel to the c-axis below the TM; this is observable only in the AP sample [42–47].

The magnetization vs. applied field M(H) measurements shown in Figure 3a were carried out at room temperature with a maximum 10 kOe applied field for all samples. The magnetization at the maximum value of the applied magnetic field (M_S) decreased when moving from AP to AO but improved in all other samples as the FiM Fe_3O_4 phase (Figure 3b). Though the M_S value decreased in the AO sample, the value did not significantly decrease, as observed with the sole α-Fe_2O_3-carrying nanostructures which have less than 10 emu/g in most cases since the sample undergoes a two-step oxidation, as explained by Zheng et al., which leaves a significant volume fraction of the FiM Fe_3O_4 phase intact [33,48,49]. Relative to bulk Fe_3O_4 with an M_S of 92 emu/g, the decrease in the M_S observed for its nanoparticle counterpart is commonly attributed to a reduction in long-range magnetic ordering and the enhancement of surface spin disorder resulting from the reduction in particle size to the nanoscale [50]. The samples did not portray superparamagnetic features, similar to the observations made by Attanayake et al., but displayed an inversely proportional relationship between the M_S and coercivity (H_C) which can be related to the Stoner–Wohlfarth theory, $H_K = (2K_{Ani})/(\mu_0 M_S)$, which shows that the magnetocrystalline anisotropy of a single-domain particle is expected to show an inversely proportional relationship between M_S and H_K; thus, we see a change in H_C in

Figure 3b [16,51,52]. The general increment in H_C in all the annealed samples may be due to the magnetic hardening of the nanostructures with annealing; this is because the magnetic phases, especially the FM/FiM phases, become more stable, with annealing making them more resistant to demagnetization; additionally, defect formation with annealing can lead to magnetic pinning, a well-known defect-engineering mechanism [53,54]. An H_C of above 100 Oe was only registered in AO, understandably due to the combination of the effects: magnetic hardening, defect formation, and increased magnetic anisotropy [5,54,55]. The tunability of the AP sample in terms of the M_S and H_C with varying gas types opens up the possibility for nanostructures to be explored for the effectiveness of magnetic hyperthermia measurements with enhanced H_C and M_S separately, further tuned in accordance to varying applications such as magnetic particle imaging and magnetic tracers [53].

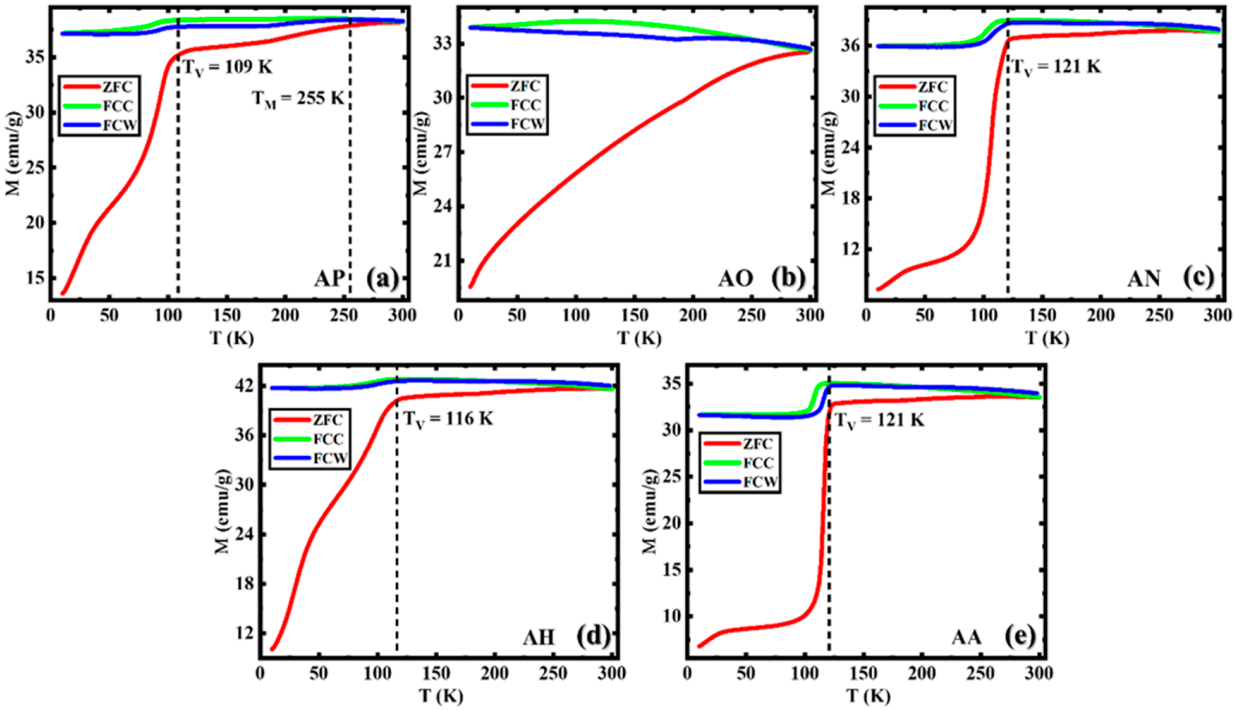

Figure 2. ZFC, FCC, and FCW M(T) curves measured in an applied field of 500 Oe for samples that were (**a**) as prepared, (**b**) annealed in O_2, (**c**) annealed in N_2, (**d**) annealed in He, and (**e**) annealed in Ar.

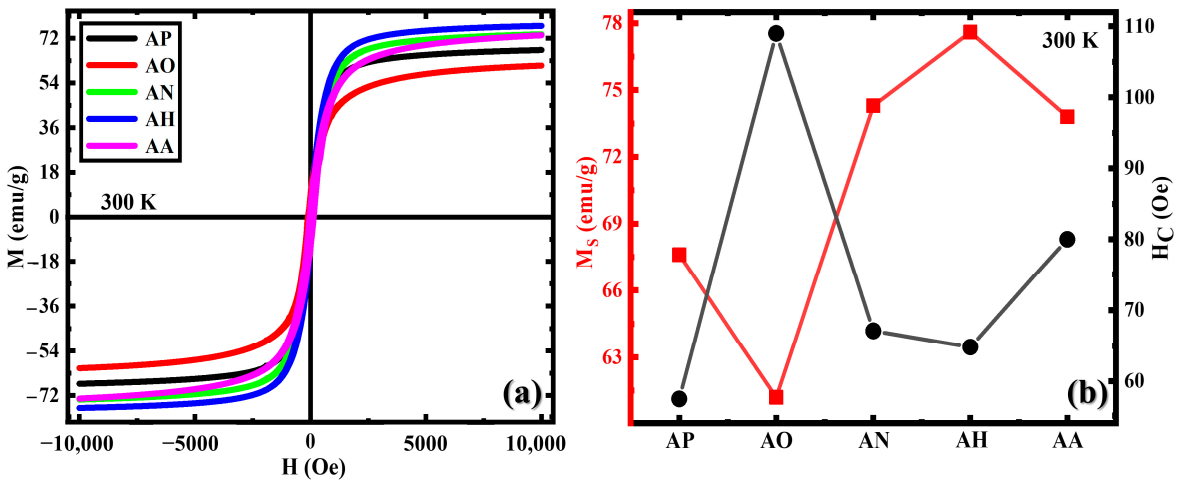

Figure 3. (**a**) Magnetic hysteresis M(H) loops of samples as prepared, annealed in O_2, annealed in N_2, annealed in He, and annealed in Ar, and (**b**) variations in magnetization at the maximum value of the applied magnetic field (M_S) and coercivity (H_C) deduced from the M(H) loops.

Low-temperature M(H) measurements at 10 K (Figure 4) showed higher M_S values compared to the 300 K typical for nanostructures as the superficial spins tend to become better aligned with the applied magnetic field at lower temperatures as the thermal energy is lower; this has been observed in smaller nanostructures with high surface-to-volume ratios, which follows Kneller's law that predicts an inversely proportional relationship between H_C and T [56,57]. The ZFC and FC protocols applied on the nanostructures did not yield an exchange bias effect at the FiM Fe_3O_4 and AFM α-Fe_2O_3 interfaces, which is understood to be due to negligible interfacial interactions due to frozen spins [16,36]. The pinning effect is observed in all samples and is the smallest in the AO sample (Figure 4b), which may be due to the formation of a γ-Fe_2O_3-like phase similar to the observations made with iron oxide nanorods annealed with oxygen [36].

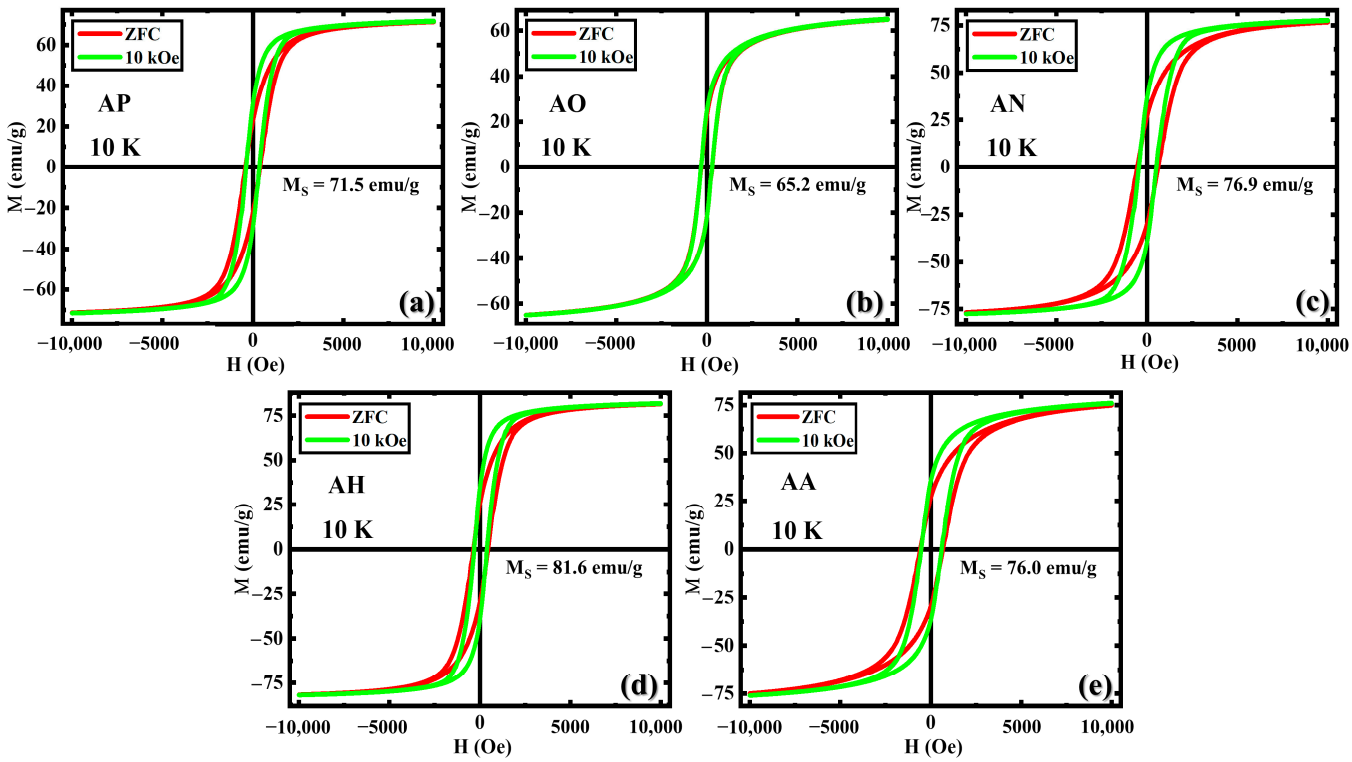

Figure 4. Magnetic hysteresis M(H) loops recorded in ZFC and FC protocols in an applied field of 10 kOe for samples (**a**) as prepared, (**b**) annealed in O_2, (**c**) annealed in N_2, (**d**) annealed in He, and (**e**) annealed in Ar.

The H_C with and without the application of the 10 kOe field shows the separation with the observed biphases (Figure 5a). The ZFC protocol which lets the spins be randomly oriented while being cooled down to a low temperature will possess a higher H_C as the antiferromagnetic exchange coupling will pin the ferrimagnetic moments at the interface, but with the application of the FC protocol, the ferrimagnetic phase will align, minimizing the interfacial pinning with the assistance of the cubic structure. The AO sample is the only sample that does not show a significant difference between the said two protocols with its dominant γ-Fe_2O_3-like phase which does not possess regular biphasic behavior in magnetic measurements. A similar observation is made in the magnetization curves in Figure 5b with AO.

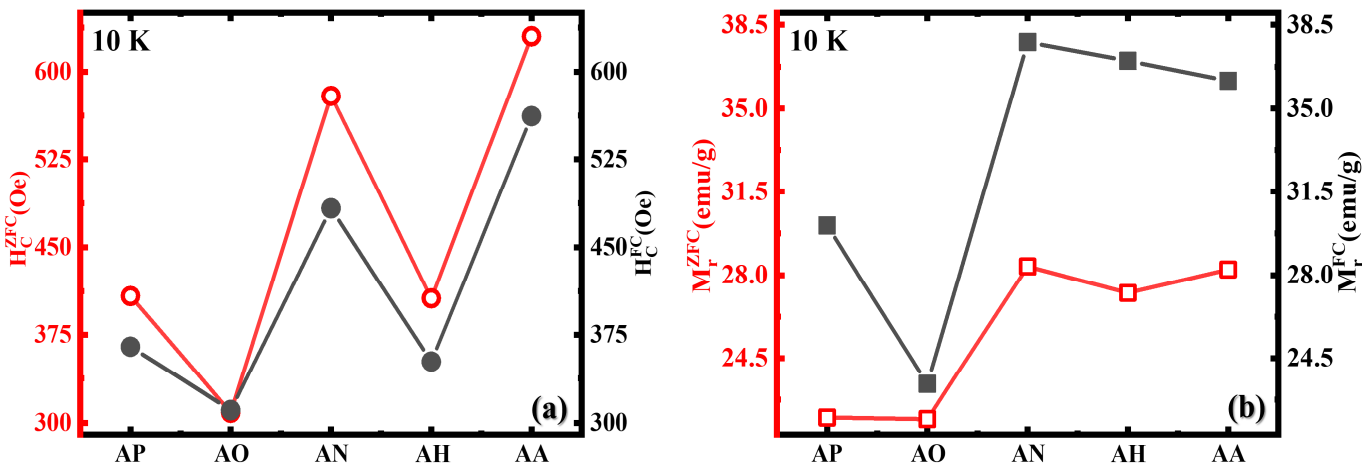

Figure 5. (**a**) H_C values obtained at 10 K for ZFC and FC configurations and (**b**) Mr at 10 K for ZFC and FC configurations.

3.3. Magnetic Hyperthermia

Figure 6a–c depicts the usage of samples in hyperthermia measurements, namely, heating T(t) curves, at varying fields for a 300 s window, which is a relatively short period that has been understood to be comparatively more effective in conjunction with radiation therapy at moderately lethal temperatures which are higher than the general hyperthermia window of 40–44 °C [58–61]. Additionally, longer treatment periods are also associated with patient fatigue, adjacent healthy tissue destruction, and changes in body condition which can lead to complex reactions, adversely affecting the health and well-being of the patient [62]. Nanoparticle introduction was kept at 1 mg/mL due to the tendency of instinctive reactions to lead to adverse conditions irrespective of compatibility [63,64]. In the in vitro study, to ensure the performance of the nanoparticles, a 2% by weight agar, a medium denser than water, was used to ensure an environment that was on par with or closer to the environment inside the body [7,65]. The SAR value of the heating curves was calculated using the initial slope of the heating curve, using the following equation;

$$SAR = \frac{\Delta T}{\Delta t}\frac{C_P}{\varphi} \quad (1)$$

The method devised assumes a homogenous sample temperature and negligible heat loss at certain time intervals at the start of the alternating magnetic field [66,67]. Here, $\Delta T/\Delta t$ gives the rate of the change in temperature, and C_P indicates the specific heat capacity of the liquid medium. Here, the agar, at 2% by weight, is assumed to have not significantly changed its specific heat capacity, which is thus 4.186 J/(g °C); the heat capacity of water is used. The symbol φ indicates the mass of the magnetic material per unit mass of liquid, which essentially gives the concentration used in the measurements.

It can be seen in Figure 6d that all the samples in general showed significant improvements in heating potential and SAR values compared to the AP sample, while the AO sample showed an exceptional enhancement. The general enhancement of heating capabilities can be due to defect enhancement and increased grain size, which lead, in turn, to increased anisotropy [53,68]. The AO sample showed the highest SAR value in all the applied magnetic fields, with the highest of 1001 W/g at 800 Oe (Figure 6d and Table 1), which is almost four times higher than that reported in FeO/Fe_3O_4 nanocubes synthesized by Khurshid et al. [18]. Further, when compared with FiM iron oxide nanocubes of a similar size synthesized by Nemati et al. which showed almost the same magnetic properties compared to the AP sample (refer Table 1), annealing was observed to have significantly increased the SAR in all the samples [6]. This suggests and re-affirms the already understood phenomena of SAR enhancement with an increasing M_S and H_C [69–71]. In our study,

34 nm nanocubes were used, eliminating variability in size and shape parameters. The adjusted annealing environments between the AO and AN samples clearly show that the M_S and H_C played a pivotal role in altering the SAR, but the enhanced H_C in the AO sample is observed to lead to a higher SAR value compared to the improved M_S in the AN sample. Table 1 summarizes the changes in the H_C, M_S, SAR, and the lattice parameter—and in all the samples—and highlights the exceptional SAR value observed in the AO sample which possessed the highest H_C, underscoring the general relation between H_C and SAR which supersedes the effect of the M_S. It is also worth mentioning that the lattice parameter (a) of sample AH, which shows the highest M_S of 77.6 emu/g, matches the value of Fe_3O_4 (8.40 Å) [23,72,73]. This highlights a correlation between the structure and magnetism of the Fe_3O_4 phase.

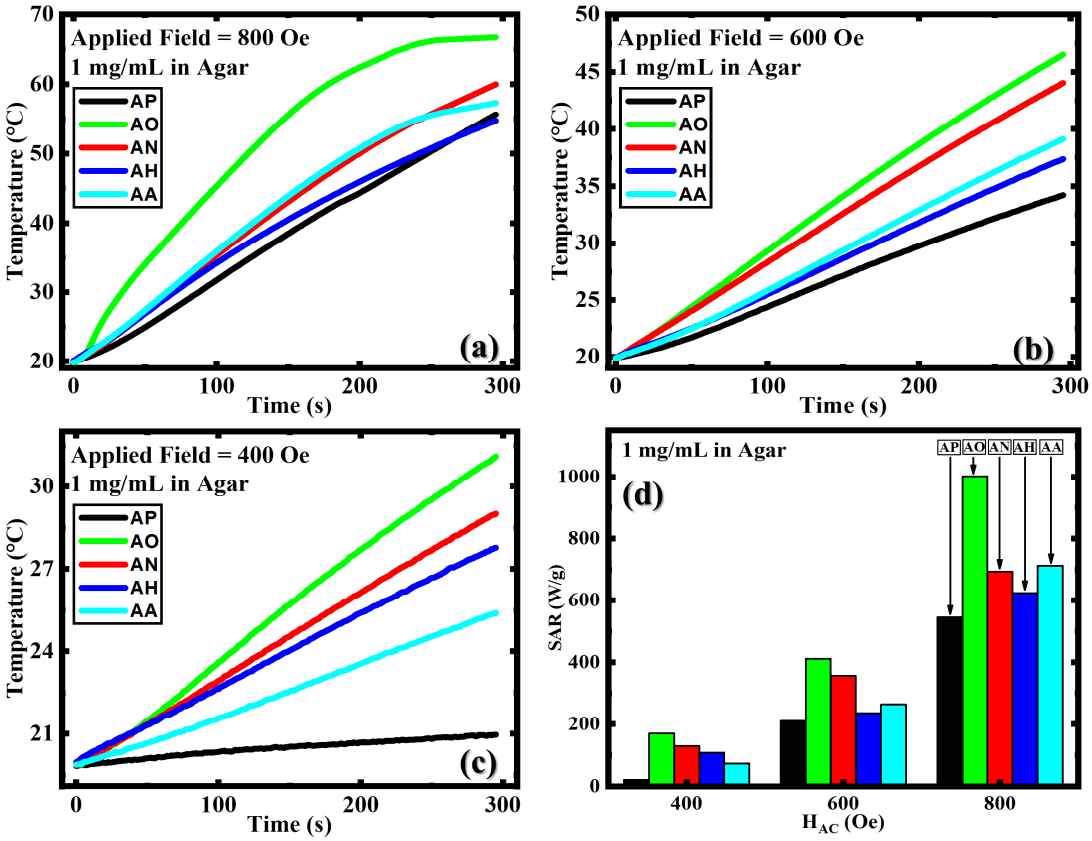

Figure 6. Heating curves of samples with 1 mg/mL concentration in agar, measured at 310 kHz frequency at (**a**) 800 Oe, (**b**) 600 Oe, (**c**) 400 Oe, and (**d**) SAR of all samples measured at 400, 600, and 800 Oe.

4. Conclusions

The phase-tunability of 34 nm iron oxide nanocubes with different types of gases enabled the enhancement of different fundamental magnetic properties, such as coercivity, saturation magnetization, and crystallinity. The enhancement of the specific absorption rate in all the samples with annealing, along with the general increment in coercivity, reflected how magnetic anisotropy can affect magnetic hyperthermia efficiency. Comparing the annealing-induced changes in coercivity and saturation magnetization, which are well-known parameters in tuning the specific absorption rate, it is observed that the former plays a larger role as the values in all the three tested applied magnetic fields were significantly higher in the AO sample with enhanced H_C. Additionally, we were able to establish a relation between the crystallinity of the structure and the enhancement of the saturation magnetization via the lattice parameter, indicating changes in the crystal structure. At low temperatures, we also observed the pinning effect in the samples.

Author Contributions: Conceptualization, S.B.A., M.-H.P. and H.S.; resources, M.-H.P. and H.S.; software, S.B.A.; investigation, S.B.A. and A.C.; formal analysis, S.B.A. and A.C.; data curation, S.B.A.; methodology, S.B.A. and R.D.; writing—original draft preparation, S.B.A.; writing—review and editing, A.C., R.D., H.S. and M.-H.P.; supervision, H.S. and M.-H.P.; project administration, H.S. and M.-H.P.; funding acquisition, H.S. and M.-H.P. All authors have read and agreed to the published version of the manuscript.

Funding: The research was supported by the US Department of Energy, and Office of Basic Energy Sciences, Division of Materials Sciences and Engineering under Award No. DE-FG02-07ER46438 and the National Science Foundation, Division of Materials Research, Solid State and Materials Chemistry Program under Award No. NSF-DMR-2327667.

Data Availability Statement: The research data will be available upon request due to privacy reasons.

Acknowledgments: The authors thank Noah Schulz for his assistance in proofreading the manuscript.

Conflicts of Interest: The authors declare no conflicts of interest.

References

1. Materón, E.M.; Miyazaki, C.M.; Carr, O.; Joshi, N.; Picciani, P.H.S.; Dalmaschio, C.J.; Davis, F.; Shimizu, F.M. Magnetic Nanoparticles in Biomedical Applications: A Review. *Appl. Surf. Sci. Adv.* **2021**, *6*, 100163. [CrossRef]
2. Martins, P.M.; Lima, A.C.; Ribeiro, S.; Lanceros-Mendez, S.; Martins, P. Magnetic Nanoparticles for Biomedical Applications: From the Soul of the Earth to the Deep History of Ourselves. *ACS Appl. Bio Mater.* **2021**, *4*, 5839–5870. [CrossRef] [PubMed]
3. Lavorato, G.C.; Das, R.; Alonso Masa, J.; Phan, M.H.; Srikanth, H. Hybrid Magnetic Nanoparticles as Efficient Nanoheaters in Biomedical Applications. *Nanoscale Adv.* **2021**, *3*, 867–888. [CrossRef] [PubMed]
4. Kons, C.; Krycka, K.L.; Robles, J.; Ntallis, N.; Pereiro, M.; Phan, M.H.; Srikanth, H.; Borchers, J.A.; Arena, D.A. Influence of Hard/Soft Layer Ordering on Magnetization Reversal of Bimagnetic Nanoparticles: Implications for Biomedical/Theranostic Applications. *ACS Appl. Nano Mater.* **2023**, *6*, 10986–11000. [CrossRef]
5. Nemati, Z.; Alonso, J.; Martinez, L.M.; Khurshid, H.; Garaio, E.; Garcia, J.A.; Phan, M.H.; Srikanth, H. Enhanced Magnetic Hyperthermia in Iron Oxide Nano-Octopods: Size and Anisotropy Effects. *J. Phys. Chem. C* **2016**, *120*, 8370–8379. [CrossRef]
6. Nemati, Z.; Alonso, J.; Rodrigo, I.; Das, R.; Garaio, E.; García, J.Á.; Orue, I.; Phan, M.H.; Srikanth, H. Improving the Heating Efficiency of Iron Oxide Nanoparticles by Tuning Their Shape and Size. *J. Phys. Chem. C* **2018**, *122*, 2367–2381. [CrossRef]
7. Das, R.; Alonso, J.; Nemati Porshokouh, Z.; Kalappattil, V.; Torres, D.; Phan, M.H.; Garaio, E.; García, J.Á.; Sanchez Llamazares, J.L.; Srikanth, H. Tunable High Aspect Ratio Iron Oxide Nanorods for Enhanced Hyperthermia. *J. Phys. Chem. C* **2016**, *120*, 10086–10093. [CrossRef]
8. Lavorato, G.C.; Das, R.; Xing, Y.; Robles, J.; Litterst, F.J.; Baggio-Saitovitch, E.; Phan, M.H.; Srikanth, H. Origin and Shell-Driven Optimization of the Heating Power in Core/Shell Bimagnetic Nanoparticles. *ACS Appl. Nano Mater.* **2020**, *3*, 1755–1765. [CrossRef]
9. Chandra, S.; Das, R.; Kalappattil, V.; Eggers, T.; Harnagea, C.; Nechache, R.; Phan, M.H.; Rosei, F.; Srikanth, H. Epitaxial Magnetite Nanorods with Enhanced Room Temperature Magnetic Anisotropy. *Nanoscale* **2017**, *9*, 7858–7867. [CrossRef]
10. Gandia, D.; Gandarias, L.; Rodrigo, I.; Robles-García, J.; Das, R.; Garaio, E.; García, J.Á.; Phan, M.H.; Srikanth, H.; Orue, I.; et al. Unlocking the Potential of Magnetotactic Bacteria as Magnetic Hyperthermia Agents. *Small* **2019**, *15*, 1902626. [CrossRef]
11. Thong, P.Q.; Huong, L.T.T.; Tu, N.D.; Nhung, H.T.M.; Khanh, L.; Manh, D.H.; Nam, P.H.; Phuc, N.X.; Alonso, J.; Qiao, J.; et al. Multifunctional Nanocarriers of Fe_3O_4@PLA-PEG/Curcumin for MRI, Magnetic Hyperthermia and Drug Delivery. *Nanomedicine* **2022**, *17*, 1677–1693. [CrossRef] [PubMed]
12. Ge, X.; Mohapatra, J.; Silva, E.; He, G.; Gong, L.; Lyu, T.; Madhogaria, R.P.; Zhao, X.; Cheng, Y.; Al-Enizi, A.M.; et al. Metal–Organic Framework as a New Type of Magnetothermally-Triggered On-Demand Release Carrier. *Small* **2023**, *20*, 2306940. [CrossRef] [PubMed]
13. Denmark, D.J.; Hyde, R.H.; Gladney, C.; Phan, M.H.; Bisht, K.S.; Srikanth, H.; Mukherjee, P.; Witanachchi, S. Photopolymerization-Based Synthesis of Iron Oxide Nanoparticle Embedded PNIPAM Nanogels for Biomedical Applications. *Drug Deliv.* **2017**, *24*, 1317–1324. [CrossRef] [PubMed]
14. Thakor, A.S.; Jokerst, J.V.; Ghanouni, P.; Campbell, J.L.; Mittra, E.; Gambhir, S.S. Clinically Approved Nanoparticle Imaging Agents. *J. Nucl. Med.* **2016**, *57*, 1833–1837. [CrossRef] [PubMed]
15. Soetaert, F.; Korangath, P.; Serantes, D.; Fiering, S.; Ivkov, R. Cancer Therapy with Iron Oxide Nanoparticles: Agents of Thermal and Immune Therapies. *Adv. Drug Deliv. Rev.* **2020**, *163–164*, 65–83. [CrossRef] [PubMed]
16. Attanayake, S.B.; Chanda, A.; Das, R.; Kapuruge, N.; Gutierrez, H.R.; Phan, M.H.; Srikanth, H. Emergent Magnetism and Exchange Bias Effect in Iron Oxide Nanocubes with Tunable Phase and Size. *J. Phys. Condens. Matter* **2022**, *34*, 495301. [CrossRef] [PubMed]
17. Martinez-Boubeta, C.; Simeonidis, K.; Makridis, A.; Angelakeris, M.; Iglesias, O.; Guardia, P.; Cabot, A.; Yedra, L.; Estradé, S.; Peiró, F.; et al. Learning from Nature to Improve the Heat Generation of Iron-Oxide Nanoparticles for Magnetic Hyperthermia Applications. *Sci. Rep.* **2013**, *3*, 1652. [CrossRef] [PubMed]

18. Khurshid, H.; Alonso, J.; Nemati, Z.; Phan, M.H.; Mukherjee, P.; Fdez-Gubieda, M.L.; Barandiarán, J.M.; Srikanth, H. Anisotropy Effects in Magnetic Hyperthermia: A Comparison between Spherical and Cubic Exchange-Coupled FeO/Fe_3O_4 Nanoparticles. *J. Appl. Phys.* **2015**, *117*, 17A337. [CrossRef]
19. Kim, D.; Lee, N.; Park, M.; Kim, B.H.; An, K.; Hyeon, T. Synthesis of Uniform Ferrimagnetic Magnetite Nanocubes. *J. Am. Chem. Soc.* **2009**, *131*, 454–455. [CrossRef]
20. Barber-Zucker, S.; Keren-Khadmy, N.; Zarivach, R. From Invagination to Navigation: The Story of Magnetosome-Associated Proteins in Magnetotactic Bacteria. *Protein Sci.* **2016**, *25*, 338–351. [CrossRef]
21. Kralj, S.; Marchesan, S. Bioinspired Magnetic Nanochains for Medicine. *Pharmaceutics* **2021**, *13*, 1262. [CrossRef] [PubMed]
22. Ju, S.; Cai, T.Y.; Lu, H.S.; Gong, C. De Pressure-Induced Crystal Structure and Spin-State Transitions in Magnetite (Fe_3O_4). *J. Am. Chem. Soc.* **2012**, *134*, 13780–13786. [CrossRef] [PubMed]
23. Lindsley, D.H. Chapter 1. The crystal chemistry and structure of oxide minerals as exemplified by the Fe-Ti oxides. In *Oxide Minerals*; De Gruyter: Berlin, Germany, 1976; pp. 1–60. [CrossRef]
24. Tokoro, H.; Fujii, S.; Oku, T. Iron Nanoparticles Coated with Boron Nitride Nanolayers Synthesized by a Solid Phase Reaction. *IEEE Trans. Magn.* **2003**, *39*, 2761–2763. [CrossRef]
25. Ling, Y.; Wang, G.; Wang, H.; Yang, Y.; Li, Y. Low-Temperature Activation of Hematite Nanowires for Photoelectrochemical Water Oxidation. *ChemSusChem* **2014**, *7*, 848–853. [CrossRef] [PubMed]
26. Rout, K.; Mohapatra, M.; Layek, S.; Dash, A.; Verma, H.C.; Anand, S. The Influence of Precursors on Phase Evolution of Nano Iron Oxides/Oxyhydroxides: Optical and Magnetic Properties. *New J. Chem.* **2014**, *38*, 3492–3506. [CrossRef]
27. Niculaes, D.; Lak, A.; Anyfantis, G.C.; Marras, S.; Laslett, O.; Avugadda, S.K.; Cassani, M.; Serantes, D.; Hovorka, O.; Chantrell, R.; et al. Asymmetric Assembling of Iron Oxide Nanocubes for Improving Magnetic Hyperthermia Performance. *ACS Nano* **2017**, *11*, 12121–12133. [CrossRef] [PubMed]
28. Le Fèvre, R.; Durand-Dubief, M.; Chebbi, I.; Mandawala, C.; Lagroix, F.; Valet, J.P.; Idbaih, A.; Adam, C.; Delattre, J.Y.; Schmitt, C.; et al. Enhanced Antitumor Efficacy of Biocompatible Magnetosomes for the Magnetic Hyperthermia Treatment of Glioblastoma. *Theranostics* **2017**, *7*, 4618. [CrossRef] [PubMed]
29. Alphandéry, E.; Chebbi, I.; Guyot, F.; Durand-Dubief, M. Use of Bacterial Magnetosomes in the Magnetic Hyperthermia Treatment of Tumours: A Review. *Int. J. Hyperth.* **2013**, *29*, 801–809. [CrossRef] [PubMed]
30. Verwey, E.J.W. Electronic Conduction of Magnetite (Fe_3O_4) and Its Transition Point at Low Temperatures. *Nature* **1939**, *144*, 327–328. [CrossRef]
31. Walz, F. The Verwey Transition—A Topical Review. *J. Phys. Condens. Matter* **2002**, *14*, R285. [CrossRef]
32. Özdemir, Ö.; Dunlop, D.J.; Moskowitz, B.M. Changes in Remanence, Coercivity and Domain State at Low Temperature in Magnetite. *Earth Planet. Sci. Lett.* **2002**, *194*, 343–358. [CrossRef]
33. Zheng, H.; Schenk, J.; Spreitzer, D.; Wolfinger, T.; Daghagheleh, O. Review on the Oxidation Behaviors and Kinetics of Magnetite in Particle Scale. *Steel Res. Int.* **2021**, *92*, 2000687. [CrossRef]
34. Anupama, A.V.; Keune, W.; Sahoo, B. Thermally Induced Phase Transformation in Multi-Phase Iron Oxide Nanoparticles on Vacuum Annealing. *J. Magn. Magn. Mater.* **2017**, *439*, 156–166. [CrossRef]
35. Attanayake, S.B.; Chanda, A.; Das, R.; Phan, M.H.; Srikanth, H. Effects of Annealing Temperature on the Magnetic Properties of Highly Crystalline Biphase Iron Oxide Nanorods. *AIP Adv.* **2023**, *13*, 025333. [CrossRef]
36. Attanayake, S.B.; Chanda, A.; Hulse, T.; Das, R.; Phan, M.-H.; Srikanth, H. Competing Magnetic Interactions and Field-Induced Metamagnetic Transition in Highly Crystalline Phase-Tunable Iron Oxide Nanorods. *Nanomaterials* **2023**, *13*, 1340. [CrossRef] [PubMed]
37. Yang, J.B.; Zhou, X.D.; Yelon, W.B.; James, W.J.; Cai, Q.; Gopalakrishnan, K.V.; Malik, S.K.; Sun, X.C.; Nikles, D.E. Magnetic and Structural Studies of the Verwey Transition in Fe3−δO4 Nanoparticles. *J. Appl. Phys.* **2004**, *95*, 7540. [CrossRef]
38. Schmitz-Antoniak, C.; Schmitz, D.; Warland, A.; Darbandi, M.; Haldar, S.; Bhandary, S.; Sanyal, B.; Eriksson, O.; Wende, H. Suppression of the Verwey Transition by Charge Trapping. *Ann. Phys.* **2018**, *530*, 1700363. [CrossRef]
39. Attanayake, S.B.; Chanda, A.; Das, R.; Phan, M.H.; Srikanth, H. Emergent Magnetic Properties of Biphase Iron Oxide Nanorods. *AIP Adv.* **2022**, *12*, 035136. [CrossRef]
40. Gaviría, J.P.; Bohé, A.; Pasquevich, A.; Pasquevich, D.M. Hematite to Magnetite Reduction Monitored by Mössbauer Spectroscopy and X-Ray Diffraction. *Phys. B Condens. Matter* **2007**, *389*, 198–201. [CrossRef]
41. Wang, W.W.; Zhu, Y.J.; Ruan, M.L. Microwave-Assisted Synthesis and Magnetic Property of Magnetite and Hematite Nanoparticles. *J. Nanopart. Res.* **2007**, *9*, 419–426. [CrossRef]
42. Artman, J.O.; Murphy, J.C.; Foner, S. Magnetic Anisotropy in Antiferromagnetic Corundum-Type Sesquioxides. *Phys. Rev.* **1965**, *138*, A912. [CrossRef]
43. Mitra, S.; Das, S.; Basu, S.; Sahu, P.; Mandal, K. Shape- and Field-Dependent Morin Transitions in Structured α-Fe_2O_3. *J. Magn. Magn. Mater.* **2009**, *321*, 2925–2931. [CrossRef]
44. Mørup, S.; Madsen, D.E.; Frandsen, C.; Bahl, C.R.H.; Hansen, M.F. Experimental and Theoretical Studies of Nanoparticles of Antiferromagnetic Materials. *J. Phys. Condens. Matter* **2007**, *19*, 213202. [CrossRef]
45. Özdemir, Ö.; Dunlop, D.J.; Berquó, T.S. Morin Transition in Hematite: Size Dependence and Thermal Hysteresis. *Geochem. Geophys. Geosystems* **2008**, *9*, 10–11. [CrossRef]
46. Shimomura, N.; Pati, S.P.; Sato, Y.; Nozaki, T.; Shibata, T.; Mibu, K.; Sahashi, M. Morin Transition Temperature in (0001)-Oriented α-Fe_2O_3 Thin Film and Effect of Ir Doping. *J. Appl. Phys.* **2015**, *117*, 17C736. [CrossRef]

47. Wang, J.; Aguilar, V.; Li, L.; Li, F.G.; Wang, W.Z.; Zhao, G. meng Strong Shape-Dependence of Morin Transition in α-Fe_2O_3 Single-Crystalline Nanostructures. *Nano Res.* **2015**, *8*, 1906–1916. [CrossRef]
48. Sun, Q.J.; Lu, X.G.; Liang, G.Y. Controlled Template-Free Hydrothermal Synthesis of Hematite Nanoplatelets. *Mater. Lett.* **2010**, *64*, 2006–2008. [CrossRef]
49. Jacob, J.; Abdul Khadar, M. VSM and Mössbauer Study of Nanostructured Hematite. *J. Magn. Magn. Mater.* **2010**, *322*, 614–621. [CrossRef]
50. Dunlop, D.J.; Ozdemir, O. *Rock Magnetism: Fundamentals and Frontiers*; Cambridge University Press: Cambridge, UK, 1997; Volume 135, p. 573. [CrossRef]
51. Chen, Q.; Zhang, Z.J. Size-Dependent Superparamagnetic Properties of $MgFe_2O_4$ Spinel Ferrite Nanocrystallites. *Appl. Phys. Lett.* **1998**, *73*, 3156–3158. [CrossRef]
52. Coore, R.R.; Love, S.; Helps, C.R.; Anil, M.H. Frequency of Brain Tissue Embolism Associated with Captive Bolt Gun Stunning of Sheep. *Foodborne Pathog. Dis.* **2004**, *1*, 291–294. [CrossRef]
53. Lak, A.; Disch, S.; Bender, P. Embracing Defects and Disorder in Magnetic Nanoparticles. *Adv. Sci.* **2021**, *8*, 2002682. [CrossRef] [PubMed]
54. Muzzi, B.; Lottini, E.; Yaacoub, N.; Peddis, D.; Bertoni, G.; De Julián Fernández, C.; Sangregorio, C.; López-Ortega, A. Hardening of Cobalt Ferrite Nanoparticles by Local Crystal Strain Release: Implications for Rare Earth Free Magnets. *ACS Appl. Nano Mater.* **2022**, *5*, 14871–14881. [CrossRef] [PubMed]
55. Singh, S.; Munjal, S.; Khare, N. Strain/Defect Induced Enhanced Coercivity in Single Domain $CoFe_2O_4$ Nanoparticles. *J. Magn. Magn. Mater.* **2015**, *386*, 69–73. [CrossRef]
56. Kneller, E.F.; Luborsky, F.E. Particle Size Dependence of Coercivity and Remanence of Single-Domain Particles. *J. Appl. Phys.* **2004**, *34*, 656. [CrossRef]
57. Nkurikiyimfura, I.; Wang, Y.; Safari, B.; Nshingabigwi, E. Temperature-Dependent Magnetic Properties of Magnetite Nanoparticles Synthesized via Coprecipitation Method. *J. Alloys Compd.* **2020**, *846*, 156344. [CrossRef]
58. Waldow, S.M.; Dougherty, T.J. Interaction of Hyperthermia and Photoradiation Therapy. *Radiat. Res.* **1984**, *97*, 380–385. [CrossRef] [PubMed]
59. Crezee, J.; Franken, N.A.P.; Oei, A.L. Hyperthermia-Based Anti-Cancer Treatments. *Cancers* **2021**, *13*, 1240. [CrossRef]
60. Kok, H.P.; Wust, P.; Stauffer, P.R.; Bardati, F.; van Rhoon, G.C.; Crezee, J. Current State of the Art of Regional Hyperthermia Treatment Planning: A Review. *Radiat. Oncol.* **2015**, *10*, 1–14. [CrossRef] [PubMed]
61. Ortega, D.; Pankhurst, Q.A. Magnetic Hyperthermia. In *Nanoscience: Volume 1: Nanostructures through Chemistry*; Royal Society of Chemistry: London, UK, 2012; pp. 60–88. [CrossRef]
62. Arora, D.; Skliar, M.; Roemer, R.B. Model-Predictive Control of Hyperthermia Treatments. *IEEE Trans. Biomed. Eng.* **2002**, *49*, 629–639. [CrossRef]
63. Moroz, P.; Jones, S.K.; Gray, B.N.; Morozy, P.; Jonesz, S.K.; Grayz, B.N. Magnetically Mediated Hyperthermia: Current Status and Future Directions. *Int. J. Hyperth.* **2002**, *18*, 267–284. [CrossRef]
64. Bellizzi, G.; Bucci, O.M.; Chirico, G. Numerical Assessment of a Criterion for the Optimal Choice of the Operative Conditions in Magnetic Nanoparticle Hyperthermia on a Realistic Model of the Human Head. *Int. J. Hyperth.* **2016**, *32*, 688–703. [CrossRef]
65. Lahiri, B.B.; Ranoo, S.; Philip, J. Effect of Orientational Ordering of Magnetic Nanoemulsions Immobilized in Agar Gel on Magnetic Hyperthermia. *J. Magn. Magn. Mater.* **2018**, *451*, 254–268. [CrossRef]
66. Andreu, I.; Natividad, E. Accuracy of Available Methods for Quantifying the Heat Power Generation of Nanoparticles for Magnetic Hyperthermia. *Int. J. Hyperth.* **2013**, *29*, 739–751. [CrossRef]
67. Hilger, I.; Frühauf, K.; Andrä, W.; Hiergeist, R.; Hergt, R.; Kaiser, W.A. Heating Potential of Iron Oxides for Therapeutic Purposes in Interventional Radiology. *Acad. Radiol.* **2002**, *9*, 198–202. [CrossRef]
68. Kayani, Z.N.; Arshad, S.; Riaz, S.; Naseem, S. Synthesis of Iron Oxide Nanoparticles by Sol-Gel Technique and Their Characterization. *IEEE Trans. Magn.* **2014**, *50*, 1–4. [CrossRef]
69. Ma, M.; Wu, Y.; Zhou, J.; Sun, Y.; Zhang, Y.; Gu, N. Size Dependence of Specific Power Absorption of Fe_3O_4 Particles in AC Magnetic Field. *J. Magn. Magn. Mater.* **2004**, *268*, 33–39. [CrossRef]
70. Mohapatra, J.; Zeng, F.; Elkins, K.; Xing, M.; Ghimire, M.; Yoon, S.; Mishra, S.R.; Liu, J.P. Size-Dependent Magnetic and Inductive Heating Properties of Fe_3O_4 Nanoparticles: Scaling Laws across the Superparamagnetic Size. *Phys. Chem. Chem. Phys.* **2018**, *20*, 12879–12887. [CrossRef] [PubMed]
71. Liu, X.L.; Fan, H.M.; Yi, J.B.; Yang, Y.; Choo, E.S.G.; Xue, J.M.; Fan, D.D.; Ding, J. Optimization of Surface Coating on Fe_3O_4 Nanoparticles for High Performance Magnetic Hyperthermia Agents. *J. Mater. Chem.* **2012**, *22*, 8235–8244. [CrossRef]
72. Klekotka, U.; Satuła, D.; Basa, A.; Kalska-Szostko, B. Importance of Surfactant Quantity and Quality on Growth Regime of Iron Oxide Nanoparticles. *Materials* **2020**, *13*, 1747. [CrossRef]
73. Panda, R.N.; Gajbhiye, N.S.; Balaji, G. Magnetic Properties of Interacting Single Domain Fe_3O_4 Particles. *J. Alloys Compd.* **2001**, *326*, 50–53. [CrossRef]

Disclaimer/Publisher's Note: The statements, opinions and data contained in all publications are solely those of the individual author(s) and contributor(s) and not of MDPI and/or the editor(s). MDPI and/or the editor(s) disclaim responsibility for any injury to people or property resulting from any ideas, methods, instructions or products referred to in the content.